

Direct magnetic imaging of fractional Chern insulators in twisted MoTe₂ with a superconducting sensor

Evgeny Redekop,¹ Canxun Zhang,¹ Heonjoon Park,² Jiaqi Cai,² Eric Anderson,² Owen Sheekey,¹ Trevor Arp,¹ Grigory Babikyan,¹ Samuel Salters,¹ Kenji Watanabe,³ Takashi Taniguchi,⁴ Xiaodong Xu,^{2,5} and Andrea F. Young^{1,*}

¹*Department of Physics, University of California, Santa Barbara, CA 93106, USA*

²*Department of Physics, University of Washington, Seattle, WA 98195, USA*

³*Research Center for Electronic and Optical Materials,
National Institute for Materials Science, 1-1 Namiki, Tsukuba 305-0044, Japan*

⁴*Research Center for Materials Nanoarchitectonics,
National Institute for Materials Science, 1-1 Namiki, Tsukuba 305-0044, Japan*

⁵*Department of Materials Science and Engineering,
University of Washington, Seattle, WA 98195, USA*

In the absence of time reversal symmetry, orbital magnetization provides a sensitive probe of topology and interactions, with particularly rich phenomenology in Chern insulators where topological edge states carry large equilibrium currents. Here, we use a nanoscale superconducting sensor [1] to map the magnetic fringe fields in twisted bilayers of MoTe₂, where transport [2, 3] and optical sensing [4, 5] experiments have revealed the formation of fractional Chern insulator (FCI) states at zero magnetic field. At a temperature of 1.6 K, we observe oscillations in the local magnetic field associated with fillings $\nu = -1, -2/3, -3/5, -4/7$ and $-5/9$ of the first moiré hole band, consistent with the formation of FCIs at these fillings. By quantitatively reconstructing the magnetization, we determine the local thermodynamic gaps of the most robust FCI state at $\nu = -2/3$, finding $^{-2/3}\Delta$ as large as 7 meV. Spatial mapping of the charge density- and displacement field-tuned magnetic phase diagram further allows us to characterize sample disorder, which we find to be dominated by both inhomogeneity in the effective unit cell area [6] as well as inhomogeneity in the band edge offset and bound dipole moment. Our results highlight both the challenges posed by structural disorder in the study of twisted homobilayer moiré systems and the opportunities afforded by the remarkably robust nature of the underlying correlated topological states.

Background

Fractional Chern insulators (FCIs) are generalizations of the fractional quantum Hall states to lattice systems with broken time reversal symmetry. Interest in FCIs arises from the fact that they may emerge as the ground state of interacting fermions on a lattice, including at zero magnetic field where time reversal symmetry is broken

spontaneously. Because FCIs are driven by electron-electron interactions, the energy gap Δ separating the incompressible ground state from its charged excitations is expected to scale with interparticle separation. In a lattice system, this is given by the inverse of the lattice constant λ , $\Delta \propto e^2/\lambda$ (where e denotes the electron charge). For sufficiently small λ , these energy gaps may be comparable to or larger than the energy gaps of fractional quantum Hall states in partially filled Landau levels at experimentally accessible magnetic fields, where the interparticle spacing is set by the magnetic length, $\ell_B \approx 25.7 \text{ nm}/\sqrt{B[\text{T}]}$.

FCIs were first observed experimentally in moiré heterostructures composed of graphene and hexagonal boron nitride (hBN) at partial fillings of topological Harper-Hofstadter bands [7] at 30 T magnetic fields; in this context the applied magnetic field plays a key role in forming the bands leading to energy gaps comparable to those observed in conventional fractional quantum Hall states. Prospects for realizing more robust lattice-based Chern insulators improved with the realization of narrow, topologically nontrivial bands at zero magnetic field in moiré systems including twisted bilayer graphene [8], rhombohedral graphene multilayers aligned to hBN [9], and transition metal dichalcogenide bilayers [10–14]. In these systems, experiments showed evidence for time reversal symmetry breaking via spontaneous valley polarization, manifesting most dramatically with the observation of quantized integer anomalous Hall effects at zero magnetic field [15–19], as well as FCI states at finite applied magnetic fields [20]. Most recently, zero magnetic field FCIs were discovered in rotationally faulted bilayers of MoTe₂ near 4° angle [2–5, 21] and in rhombohedral graphene pentalayers aligned to a hBN substrate [22]. These observations raise key questions about the microscopic origin of these states, their competition with other correlated ground states, and the possibility for realizing novel topological phases absent in partially filled Landau levels, leading to a growing body of theoretical work [23–31].

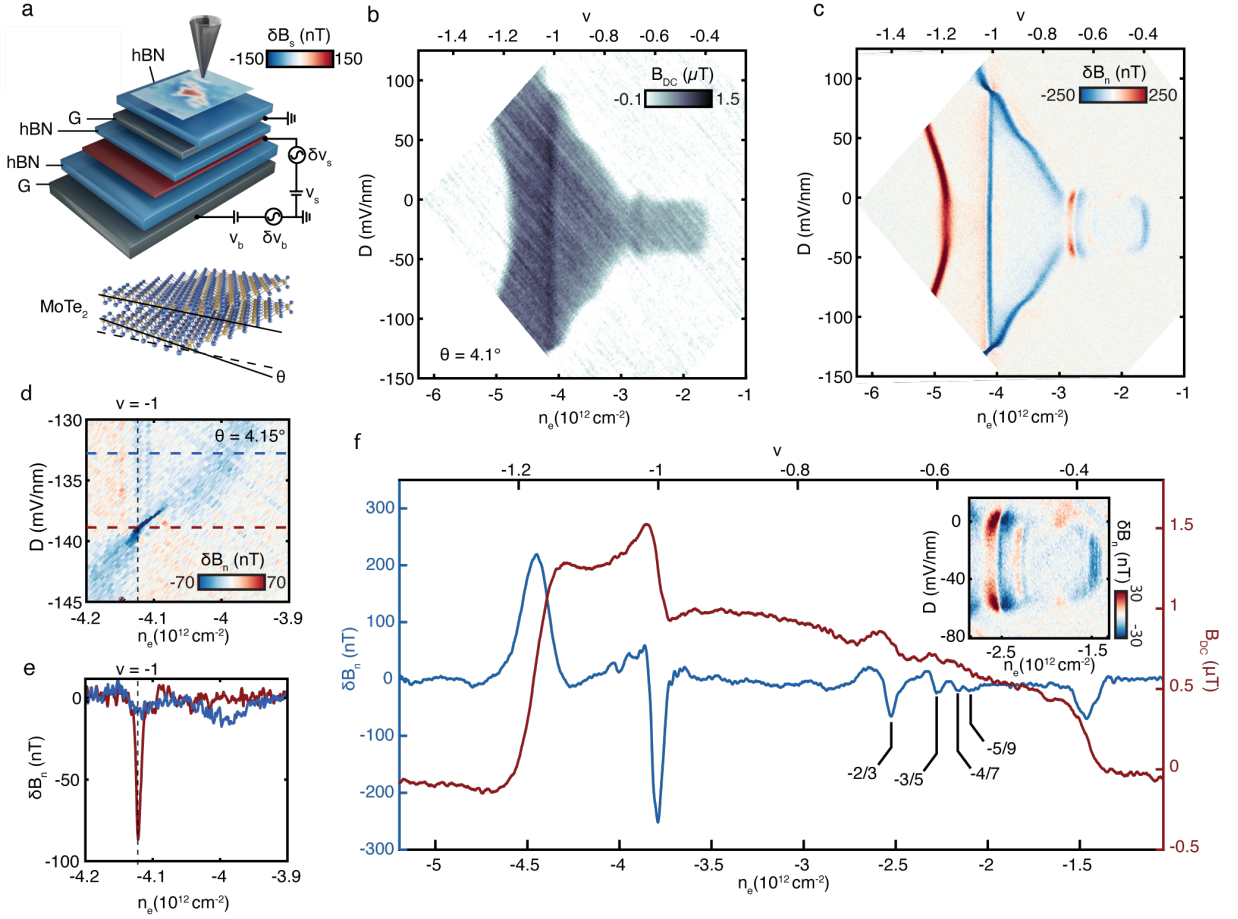


FIG. 1. **Local magnetometry of FCIs in twisted MoTe₂.** (a) Schematic of the experimental geometry, showing a nSOT sensor above a van der Waals heterostructure consisting of a dual graphite-gated MoTe₂ bilayer with nominal $\theta = 3.9^\circ$ misalignment angle. Static voltages V_s and V_b and modulated voltages δV_s and δV_b are applied to the sample and bottom gate as shown, allowing finite-frequency readout of the modulated magnetization, shown in overlay for finite δV_s and $\delta V_b = 0$ at moiré filling $\nu = -1$ in Sample B. (b) Static magnetic field B_{DC} measured at a single point as a function of charge carrier density n_e and applied electric displacement field D at 1.6 K in Sample A. (c) δB_n with an applied modulation of $\delta n \approx 1.5 \times 10^{10} \text{ cm}^{-2}$, measured at the same position as data in panel b. (d) δB_n measured with $\delta n \approx 1.5 \times 10^9 \text{ cm}^{-2}$ near the valley polarization transition at $\nu = -1$. The sharp signal is indicative of a first-order phase transition where the magnetization vanishes. (e) Two traces extracted from panel d. (f) δB_n and B_{DC} measured at $T = 1.6 \text{ K}$, $B = 34 \text{ mT}$ and $D = -30 \text{ mV/nm}$; for δB_n the applied $\delta n \approx 1.2 \times 10^{10} \text{ cm}^{-2}$. We identify the peak at $\nu \approx -1.175$ and dip at $\nu \approx -0.39$ with the boundaries of the magnetic phase, and the five minima at $\nu = -1, -2/3, -3/5, -4/7,$ and $-5/9$ with the edge state magnetization of Chern insulator states. Inset: δB_n measured with an applied modulation $\delta n \approx 1.5 \times 10^9 \text{ cm}^{-2}$ in the FCI regime, showing D -independent minima at $\nu = -2/3$ and $-3/5$ within the valley-polarized regime.

Local magnetometry of fractional Chern insulators

Here we take advantage of the compatibility of zero-magnetic field FCIs with superconducting sensors to perform ultrasensitive magnetometry of the fringe magnetic fields associated with spin and orbital magnetism in twisted MoTe₂ on the submicron scale. In a Chern insulator, equilibrium currents carried by the chiral edge states contribute a topological magnetization

$$\Delta m = \frac{C\Delta}{\Phi_0}, \quad (1)$$

which represents the change in magnetization across the incompressible bulk gap (here C is the total Chern number, Δ is the thermodynamic energy gap, and Φ_0 is the non-superconducting flux quantum). This universal contribution occurs atop a non-universal background of spin and orbital magnetic moments arising from the filled electronic states in the sample bulk. Previous experiments have used nanoscale superconducting quantum interference device on tip (nSOT) [32, 33] to detect orbital currents associated with the formation of integer quantum Hall states in monolayer graphene [6], quantum anomalous Hall states in both graphene and dichalcogenide

moiré systems [34, 35], and the non-topological orbital magnetization associated with orbitally polarized metallic states in both moiré and non-moiré graphene systems [36, 37]. However, magnetic imaging of fractionalized phases has not been reported.

We use an indium nSOT sensor with effective diameter of approximately 200 nm to map the fringe magnetic field above several twisted bilayer MoTe₂ samples. Our sensors represent a significant improvement over the state-of-the-art [33], with a measured sensitivity of $0.2 \text{ nT}/\sqrt{\text{Hz}}$ (see Extended Data Fig. 1 and Methods) corresponding to $4n\Phi_0/\sqrt{\text{Hz}}$, where Φ_0 is the superconducting flux quantum. Our samples consist of a twisted bilayer MoTe₂ active layer encapsulated by hBN dielectrics with graphite top and bottom gates (see Fig. 1a and Extended Data Fig. 2). Together, the gates allow independent control of the charge carrier density n_e and electric displacement field D . The graphite gates are transparent to the fringe magnetic fields, making magnetic imaging an ideal tool for probing the n_e and D -tuned phase diagram. We measure the fringe fields either in direct current mode via the static magnetic field B_{DC} at fixed n and D or in alternating current mode through lock-in readout of the magnetic response to modulations applied to the sample and/or top and bottom gate voltages. Appropriate choice of the relative magnitude and phase of these voltages allows us to measure either the density- or displacement field derivatives of the fringe field, $\delta B_n \approx \frac{\partial B_{\text{DC}}}{\partial n_e} \delta n_e$ and $\delta B_D \approx \frac{\partial B_{\text{DC}}}{\partial D} \delta D$.

Figure 1b shows B_{DC} measured locally at a height 50 nm above the surface of sample A. Magnetic signal is observed in a broad region of the phase diagram centered at low displacement field, consistent with previous optical and transport measurements [2, 5, 19]. We associate this regime with a valley-imbalanced ferromagnetic phase. Features previously identified as Chern insulators at $\nu = -1$ and $\nu = -2/3$ are visible in this image as subtle vertical lines. These become plainly visible in measurements of δB_n , shown in Fig. 1c. In this contrast mode, the *decrease* in magnetization with *increasing* chemical potential, characteristic of the edge states of Chern insulators with negative C , manifests as a sharp, negative (blue) signal that appears at a D -independent density. Similar phase diagrams were obtained from three samples, as shown in Extended Data Fig. 2. The charge carrier density in the tMoTe₂ may be independently calibrated using magnetic features associated with Landau levels in the graphite top gate, and measurements in Device C confirm that the negative δB_n feature associated with the $\nu = -2/3$ state occurs at filling factor $\nu = 0.66 \pm .02$ (see Extended Data Fig. 3).

Our high sensitivity local measurement allows us to examine several aspects of the phase diagram that have been ambiguous in previous studies of the same system. For example, we find that, while the signal associated

with the Chern insulator gap is the strongest at zero effective displacement field (see Extended Data Fig. 4), it remains finite until the sharp, D -tuned phase transition to a non-magnetic phase. This is confirmed by low excitation, high resolution measurements of δB_n in the vicinity of the phase transition at large negative D shown in Fig. 1d, where an exceptionally sharp feature associated with a decrease in magnetization appears at $\nu = -1$. As shown in Fig. 1e, the fringe magnetic field associated with this feature is about one order of magnitude larger than those associated with the Chern insulator edge states at $\nu = -1$, and the large negative signal occurs over a narrow range of D and n_e . This is expected for a first order phase transition between a valley-imbalanced Chern insulator and a topologically trivial insulator with no net magnetization (see additional data in Extended Data Fig. 5). We conclude that the first order phase transition in valley polarization occurs before any displacement field-tuned change in band topology, and find no evidence for a valley-imbalanced metallic state. Notably, while the valley-imbalanced transition is sharp at $\nu = -1$, where the transition occurs between a Chern insulator and topologically trivial correlated insulator[2], it is broad in the metallic regimes between commensurate filling factors.

Figure 1f shows a high resolution trace of both B_{DC} and δB_n acquired at $T = 1.6 \text{ K}$, $B = 34 \text{ mT}$ and $D = -30 \text{ mV/nm}$. In this dataset, we observe oscillations in the local magnetic field, with oscillation minima associated with band fillings $\nu = -1, -2/3, -3/5, -4/7$ and $-5/9$. High resolution data acquired near filling $\nu = -1/2$ as a function of both n_e and D (Fig. 1f, inset) shows negative δB_n features at $\nu = -2/3$ and $\nu = -3/5$, which (mimicking the behavior at $\nu = -1$) persist to the valley polarization transition. We associate the negative features with the FCI gaps; notably, however, they are accompanied by a positive δB_n feature at slightly higher hole density. We associate this feature with a non-topological magnetization that arises for small doping of the system away from the FCI gaps.

Current theoretical understanding of twisted bilayer MoTe₂ suggests that the single-particle wave functions of the lowest energy moiré hole band in a single valley resemble those of the lowest energy Landau level in a two-dimensional electron system, with an emergent composite Fermi liquid state at half filling [23, 31]. As in fractional quantum Hall systems in partially filled Landau levels, then, a sequence of incompressible states are observed at fillings $p/(2p \pm 1)$ corresponding to the quantum oscillations of the composite fermions in the effective magnetic field [38], which in this case is completely interaction induced property of the magnetic ground state. In this picture, the oscillations we observe in the *physical* fringe magnetic field as a function of the density may be associated with de Haas-van Alphen oscillations of the composite fermions in the *emergent* magnetic field. Our obser-

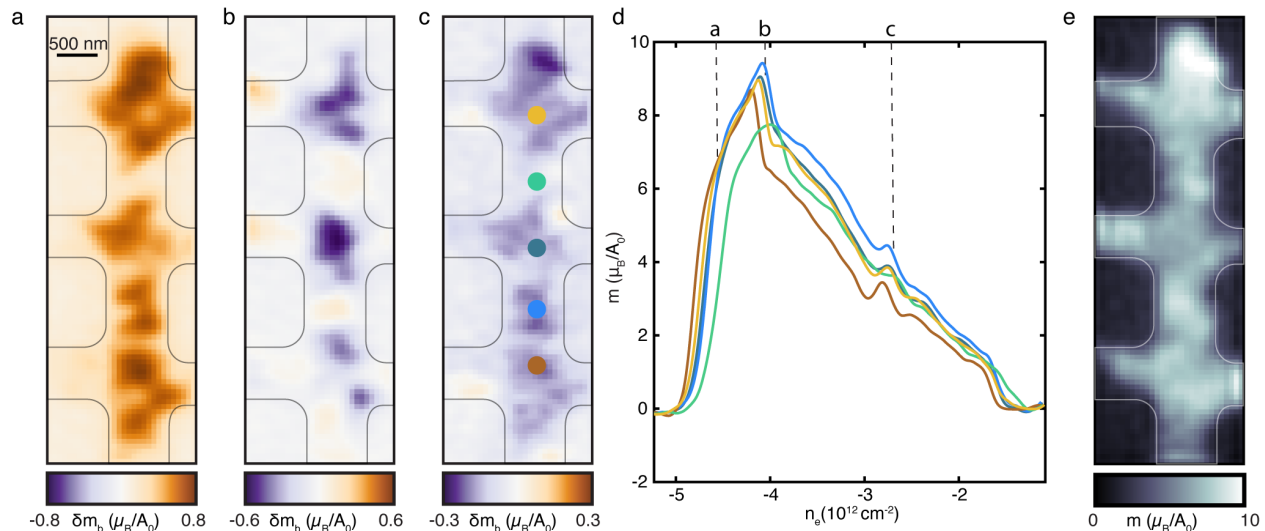


FIG. 2. **Reconstructing local magnetization.** (a) Differential magnetization δm_b reconstructed from spatial maps of $\delta B_b \approx (\partial B/\partial V_b)\delta V_b$, measured at $D = -30$ mV/nm and density corresponding to $\nu \approx -1.2$, (b) $\nu \approx -1$, and (c) $\nu \approx -0.66$. Here $A_0 = 23.7$ nm² is the superlattice unit cell area corresponding to a twist angle of 3.89°. (d) Total out-of-plane magnetization m , calculated by integrating the differential magnetization for the spatial positions indicated in panel c. (e) Spatial image of m at $D = -30$ mV/nm and $\nu = -1.12$.

variation of oscillations in the magnetization, $m = dF/dB$, can be taken as direct evidence for the emergence of topological gaps whose charge density is magnetic field dependent.

Quantifying local magnetization

The data shown in Fig. 1 provides a qualitative picture of the microscopic phase diagram. To quantitatively measure the magnetization, we take spatial scans of B_{DC} and δB_b and use an inversion algorithm to reconstruct the static magnetization m and differential magnetization change in response to a change in bottom gate voltage, $\delta m_b = \partial m/\partial V_b \times \delta V_b$ (see Methods and Extended Data Fig. 6). This analysis assumes that magnetic moments point only in the out-of-plane direction, an assumption that is well justified in strongly spin-orbit coupled twisted MoTe₂. Figures 2a, b and c show δm_b images acquired at applied $D = -30$ mV/nm and n_e corresponding to $\nu \approx -1.1$, $\nu \approx -1$ and $\nu \approx -2/3$ respectively. The sample magnetization is inhomogeneous on submicron scales, a feature universal to all samples measured. Figure 2d shows the n_e -dependent total m , obtained by integrating δm_b , at several different points in the device shown in Fig. 2c. These data are consistent with a large, non-topological orbital magnetization in the ferromagnetic phase ranging from 6 to 8 Bohr magnetons (μ_B) per hole. This agrees with estimates for the renormalization of the spin moment arising from atomic scale spin-orbit coupling determined from band theory and optical exper-

iments [39–41]. Despite the strong spatial inhomogeneity in the internal structure of the ferromagnetic region, the entire sample is magnetized, consistent with valley polarization being a robust feature of the phase diagram across a range of sample parameters (Fig. 2e).

Our quantitative reconstruction of the magnetization may also be used to directly determine the Chern insulator gaps via Eq. (1). Figures 3a-b show m in the vicinity of $\nu = -1$ and $\nu = -2/3$. We extract the change in magnetization from the extent of the negative-slope regions at each rational filling factor, obtaining $\Delta m_{-1} = 1.4(1) \mu_B/\text{u.c.}$ and $\Delta m_{-2/3} = 0.46(3) \mu_B/\text{u.c.}$ Assuming $C = \nu$ (consistent with transport measurements of the same sample [2]), this yields thermodynamic energy gaps of $^{-1}\Delta = 14(1)$ meV and $^{-2/3}\Delta = 7.0(5)$ meV.

The ranges in measured gap sizes reflect the spread in measured values in the small area outlined in red in Figs. 3a-b, rather than experimental uncertainty. Our determination of the gap sizes is, however, susceptible to several sources of error. While some uncertainty is contributed by the calibration of our magnetometer (which we measure to a reproducibility of approximately 5%), systematic errors are likely more significant. One source of error arises from the fact that our measurement window does not capture the entire region of the physical magnetic field. Because magnetic dipole fields are long-range, the magnetic inversion algorithm takes as an input both the field in the measured region and an assumed field outside the measured region; in the data shown in the main text, this field is assumed to be zero. To estimate the magnitude of the error resulting from this as-

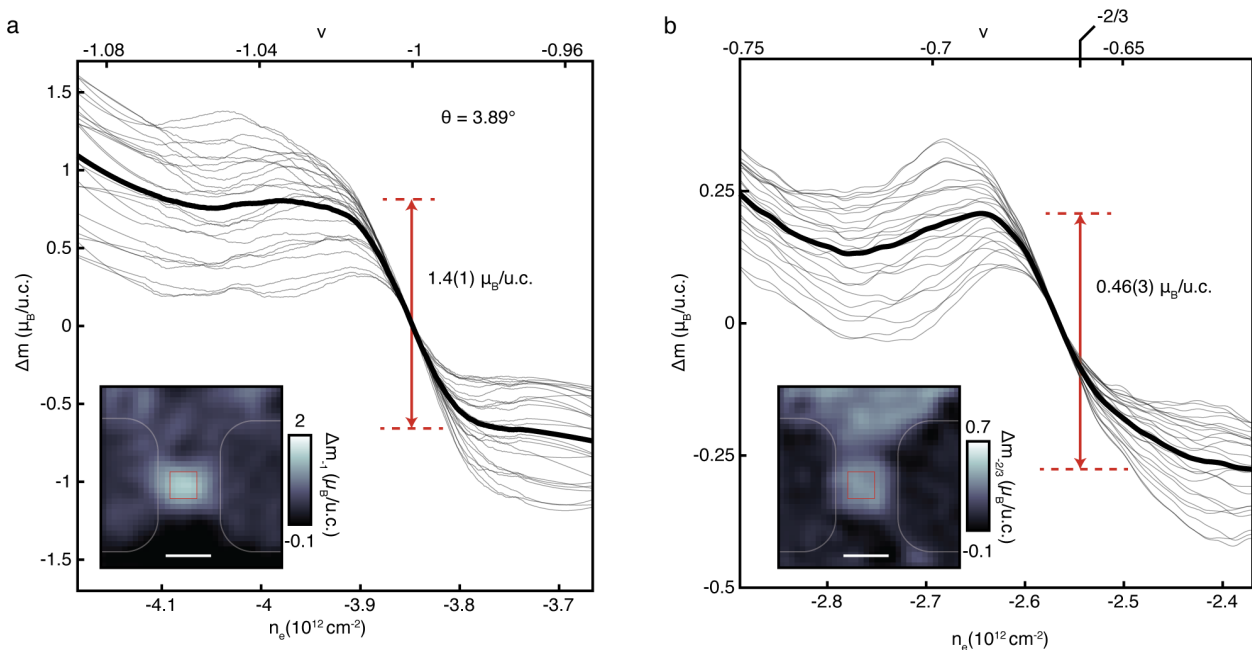


FIG. 3. **Thermodynamic gaps.** (a) Magnetization change Δm (referenced to the center of the $\nu = -1$ gap) in a region where the local twist angle $\theta \approx 3.89^\circ$. The inset shows a spatial scan of Δm_{-1} the difference in magnetization on the boundaries of the Chern insulator at $\nu = -1$. We find a change of $\Delta m_{-1} = 1.4(1) \mu_B/u.c.$ across $\nu = -1$, corresponding to $^{-1}\Delta = 14(1)$ meV gap for $C = -1$. (b) m for $\nu = -2/3$ (referenced to the center of the $\nu = -2/3$ gap), measured in the same grid points. Inset shows the difference in magnetization on the boundaries of the Chern insulator at $\nu = -2/3$. $\Delta m_{-2/3} = 0.46(3) \mu_B/u.c.$, corresponding to thermodynamic gap $^{-1}\Delta = 7.0(5)$ meV, assuming $C = -2/3$.

sumption, we compare m calculated using ‘zero-padding’ to calculations done with different physically motivated padding assumptions (see methods and Extended Data Fig. 7). Across several models, we find that m is consistent to within 10%. A second source of uncertainty is conceptual, and arises from our empirical definition of the thermodynamic gap, where we assume that the region of steepest negative slope in m arises entirely from the chiral edge states. While this is known to be true in the clean limit for fractional Hall states in partially filled Landau levels, theoretical calculations accounting for the effects of finite disorder and inhomogeneous Berry curvature are not available to justify this empirical definition of the thermodynamic energy gap.

In a clean quantum Hall system, the thermodynamic gap measures the energy to add one electron of charge to the gapped ground state. In states whose excitations carry only integer charge, this is equivalent to the thermal activation gap. In states whose elementary excitations carry fractional charge $e^* = e/q$, however, the thermal activation gap measured in transport is expected to be smaller than the thermodynamic gap by a factor of q . In a disorder-free, partially filled Landau level with Coulomb interactions, the ratio of the thermodynamic gaps at $\nu = 1$ and $\nu = 1/3$ is expected to be approximately 4[42]; we find a ratio of approximately 2—i.e., the fractional state is larger in compar-

ison to the integer state than for a Landau level system. Our data also show a notable when compared with transport measurements. From our measurements, $^{-1}\Delta$ corresponds to a thermal activation gap of 150 K, approximately five times larger than the 30 K found in transport measurements[2]. However, our measurement of $^{-2/3}\Delta \approx 7$ meV corresponds to an estimated thermal activation gap of approximately 27 K, roughly *consistent* with transport measurements[2]. Quantitatively reconciling these observations requires a detailed theory that accounts for both band effects unique to lattice Chern bands as well as the contrasting effects of disorder on the thermodynamic and transport gaps at integer and fractional filling.

As a final point of comparison, the energy scales measured here are also similar in scale to thermodynamic gaps measured in monolayer graphene fractional quantum Hall systems at $B \approx 14$ T in a similar electrostatic geometry [43]. We note, however, that sample inhomogeneity on length scales smaller than that of our local probe may well contribute to the lowering of the measured thermodynamic gaps in twisted MoTe₂ relative to the intrinsic gap size. The intrinsic gaps may thus be even larger than reported here, consistent with theoretical analyses that find MoTe₂ bilayers to be equivalent to conventional quantum Hall states at magnetic fields as large as 160 T [23].

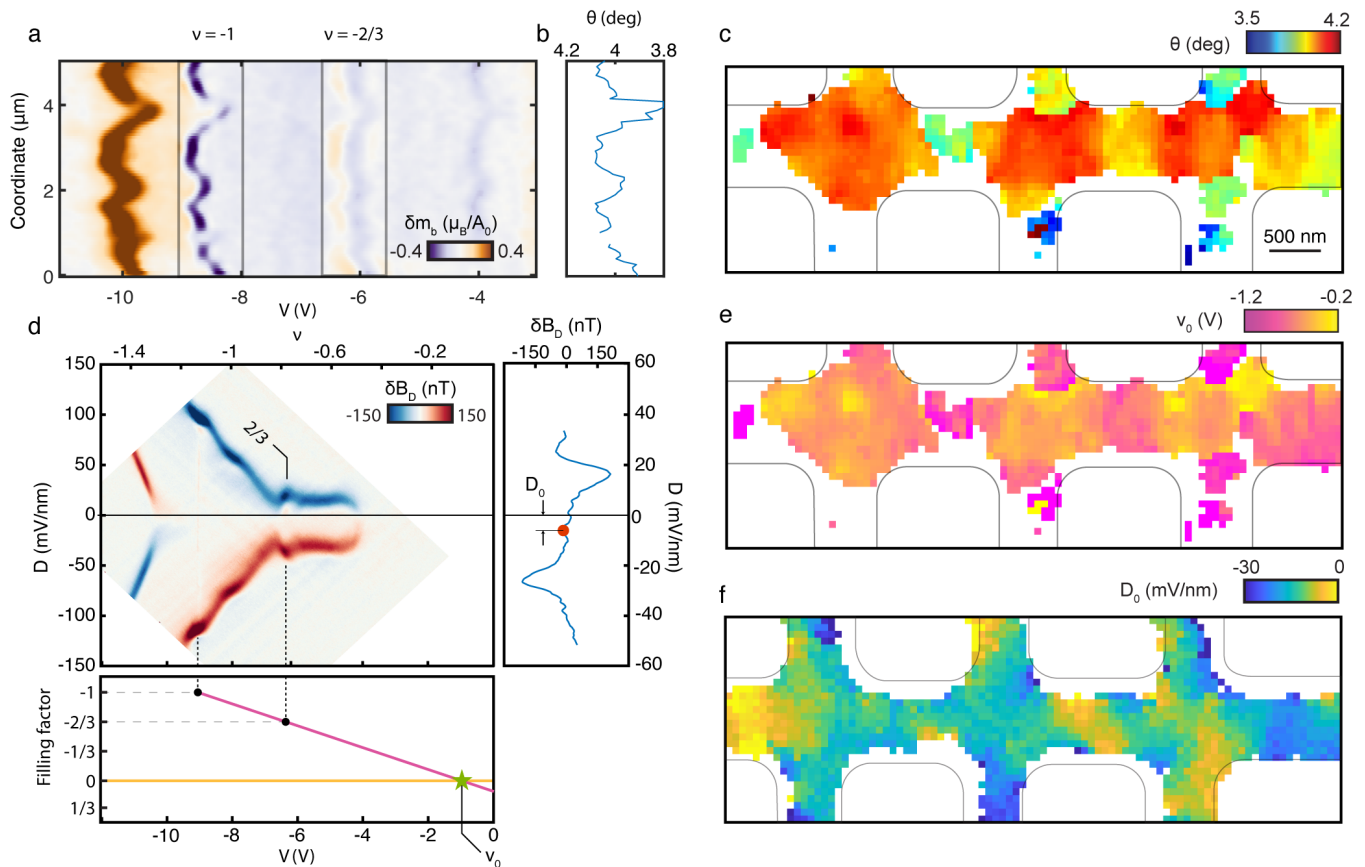


FIG. 4. **Sources of disorder.** (a) δm_b as a function $V \equiv V_T + V_B$ along a trajectory running along the center of the device. Features near $V = -9$ V and -6 V correspond to topological gaps at $\nu = -1$ and $\nu = -2/3$, respectively. (b) Effective interlayer twist angle along the spatial trajectory of panel a, extracted from the density difference between $\nu = -1$ and $\nu = -2/3$ magnetization features. (c) Local twist angle map in device A. (d) δB_D as a function of V and D . In addition to the twist angle, the voltages corresponding to Chern insulators at $\nu = -1$ and $\nu = -2/3$ are used to extract the valence band offset, V_0 , corresponding to $n_e = 0$. The D -induced valley-polarization transitions, meanwhile, are used to extract the displacement field offset D_0 . (e) Spatial map of V_0 in device A. (f) Spatial map D_0 in device A.

Sources of disorder in twisted MoTe_2

A key consideration in the interpretation of both transport and bulk thermodynamic data in moiré systems is sample disorder. In particular, variations in structural parameters can make the same Chern insulator state occur at different values of the applied gate voltages in different parts of the sample; the sample will then not be uniformly gapped and measurements will be strongly dependent on the size and shape of the probed region. Macroscopic thermodynamic probes average both incompressible and compressible regions, reducing the measured thermodynamic gap, while transport measurements may see edge state transport shorted by bulk conducting regions of the sample. The effect of structural disorder is evident in Fig. 4a, which shows δm_b as a function of the sum of the applied gate voltages to the top and bottom gates, $V \equiv V_t + V_b$ (with D held constant) and the spatial coordinate along a trajectory that

runs along the ‘spine’ of the Hall bar sample. The applied gate voltage required to reach the same moiré density varies by $\approx 10\%$. As the Chern insulator states at $\nu = -1$ and $\nu = -2/3$ occur at fixed, known filling of the moiré superlattice, the voltages at which they appear allow us to extract the ‘moiré density’, defined as $n_M^{-1} = \frac{\sqrt{3}a^2}{2\sin(\theta)}$ via the relation $c(V_{-1} - V_{-2/3}) = n_M/3$ where c is the capacitance per unit area of the two gates. The effective interlayer twist angle θ corresponding to the trajectory in Fig. 4a is plotted in Fig. 4b, while a map of the effective twist angle throughout the device is shown in Fig. 4c. Qualitatively, the twist angle map is reminiscent of twisted bilayer graphene [6] with regions of approximately uniform twist angle separated by domain walls where the effective twist angle changes suddenly.

We also identify additional microscopic sources of disorder. Fig. 4d shows a measurements of δB_D as a function of D and V . In addition to the twist angle, V_{-1} and $V_{-2/3}$ also allow us to determine the threshold voltage as-

sociated with the valence band edge, $V_0 = 3V_{-2/3} - 2V_{-1}$. This quantity, which we term the band edge offset, may be determined by the band gap of the MoTe₂ layers as well as bound electric charges (for example in an impurity band) which must be filled before the first itinerant hole populates the MoTe₂ valence band. Fig. 4e shows a spatial map of this quantity, which varies by as much as one volt across the sample. Variations in this parameter are confirmed by chemical potential sensing measurements that leverage the magnetic response of the top graphite gate (see Extended data Fig. 3). We also find evidence for a built-in dipole moment. As shown in Fig. 4d, the ferromagnetic region of the phase diagram is symmetric about a fixed but non-zero value of D . We associate this displacement field offset D_0 with a built-in electric field, which we find varies spatially on the micron scale as shown in Fig. 4f. This electric field may be associated with heterostrain in the MoTe₂ bilayer, which breaks the layer-inversion symmetry of the idealized bilayer system at $D = 0$ mV/nm and induces bound dipole charge within the layers. Despite these sources of inhomogeneity, FCI states are observed over most of the sample area, suggesting a certain degree of robustness of the underlying phenomena.

Conclusion

In conclusion, our results highlight both the promise and challenges of twisted homobilayer moiré materials for the study of FCI physics. On one hand, sizes of the measured FCI gaps make twisted MoTe₂ one of the most robust fractional quantum Hall systems studied. On the other hand, the strong spatial inhomogeneity poses a challenge for future experiments. Interferometric detection of quasiparticle statistics [44], for example, typically requires highly uniform two-dimensional electron systems where the trajectory of the current-carrying edge states can be precisely controlled.

Acknowledgments

The authors thank Liang Fu, Taige Wang, and Michael Zaletel for discussions. Work at UCSB was primarily supported by the Army Research Office under award W911NF-20-2-0166. E.R. and O.S. acknowledge support by the National Science Foundation through Enabling Quantum Leap: Convergent Accelerated Discovery Foundries for Quantum Materials Science, Engineering and Information (Q-AMASE-i) award number DMR-1906325. A.F.Y. acknowledges additional support by the Gordon and Betty Moore Foundation EPIQS program under award GBMF9471. The work at University of Washington is supported by DoE BES under award DE-SC0018171. Device fabrication used the facilities

and instrumentation supported by NSF MRSEC DMR-230879. K.W. and T.T. acknowledge support from the Elemental Strategy Initiative conducted by the MEXT, Japan (Grant Number JPMXP0112101001) and JSPS KAKENHI (Grant Numbers 19H05790, 20H00354 and 21H05233).

COMPETING INTERESTS

The authors declare no competing interests.

DATA AVAILABILITY

The data that support the plots within this paper are available from the corresponding author upon reasonable request.

* andrea@physics.ucsb.edu

- [1] A. Finkler, Y. Segev, Y. Myasoedov, M. L. Rappaport, L. Ne'eman, D. Vasyukov, E. Zeldov, M. E. Huber, J. Martin, and A. Yacoby, *Nano Letters* **10**, 1046 (2010).
- [2] H. Park, J. Cai, E. Anderson, Y. Zhang, J. Zhu, X. Liu, C. Wang, W. Holtzmann, C. Hu, Z. Liu, T. Taniguchi, K. Watanabe, J.-H. Chu, T. Cao, L. Fu, W. Yao, C.-Z. Chang, D. Cobden, D. Xiao, and X. Xu, *Nature* **622**, 74 (2023).
- [3] F. Xu, Z. Sun, T. Jia, C. Liu, C. Xu, C. Li, Y. Gu, K. Watanabe, T. Taniguchi, B. Tong, J. Jia, Z. Shi, S. Jiang, Y. Zhang, X. Liu, and T. Li, *Physical Review X* **13**, 031037 (2023).
- [4] J. Cai, E. Anderson, C. Wang, X. Zhang, X. Liu, W. Holtzmann, Y. Zhang, F. Fan, T. Taniguchi, K. Watanabe, Y. Ran, T. Cao, L. Fu, D. Xiao, W. Yao, and X. Xu, "Signatures of Fractional Quantum Anomalous Hall States in Twisted MoTe2 Bilayer," (2023).
- [5] Y. Zeng, Z. Xia, K. Kang, J. Zhu, P. Knüppel, C. Vaswani, K. Watanabe, T. Taniguchi, K. F. Mak, and J. Shan, *Nature* **622**, 69 (2023).
- [6] A. Uri, S. Grover, Y. Cao, J. A. Crosse, K. Bagani, D. Rodan-Legrain, Y. Myasoedov, K. Watanabe, T. Taniguchi, P. Moon, M. Koshino, P. Jarillo-Herrero, and E. Zeldov, *Nature* **581**, 47 (2020).
- [7] E. M. Spanton, A. A. Zibrov, H. Zhou, T. Taniguchi, K. Watanabe, M. P. Zaletel, and A. F. Young, *Science* **360**, 62 (2018).
- [8] Y. Cao, V. Fatemi, A. Demir, S. Fang, S. L. Tomarken, J. Y. Luo, J. D. Sanchez-Yamagishi, K. Watanabe, T. Taniguchi, E. Kaxiras, R. C. Ashoori, and P. Jarillo-Herrero, *Nature* **556**, 80 (2018).
- [9] G. Chen, L. Jiang, S. Wu, B. Lyu, H. Li, B. L. Chittari, K. Watanabe, T. Taniguchi, Z. Shi, J. Jung, Y. Zhang, and F. Wang, *Nature Physics* **15**, 237 (2019).
- [10] E. C. Regan, D. Wang, C. Jin, M. I. Bakti Utama, B. Gao, X. Wei, S. Zhao, W. Zhao, Z. Zhang, K. Yumigeta, M. Blei, J. D. Carlström, K. Watanabe,

- T. Taniguchi, S. Tongay, M. Crommie, A. Zettl, and F. Wang, *Nature* **579**, 359 (2020).
- [11] Y. Tang, L. Li, T. Li, Y. Xu, S. Liu, K. Barmak, K. Watanabe, T. Taniguchi, A. H. MacDonald, J. Shan, and K. F. Mak, *Nature* **579**, 353 (2020).
- [12] L. Wang, E.-M. Shih, A. Ghiotto, L. Xian, D. A. Rhodes, C. Tan, M. Claassen, D. M. Kennes, Y. Bai, B. Kim, K. Watanabe, T. Taniguchi, X. Zhu, J. Hone, A. Rubio, A. N. Pasupathy, and C. R. Dean, *Nature Materials* **19**, 861 (2020).
- [13] Y. Shimazaki, I. Schwartz, K. Watanabe, T. Taniguchi, M. Kroner, and A. Imamoğlu, *Nature* **580**, 472 (2020).
- [14] Y. Xu, S. Liu, D. A. Rhodes, K. Watanabe, T. Taniguchi, J. Hone, V. Elser, K. F. Mak, and J. Shan, *Nature* **587**, 214 (2020).
- [15] A. L. Sharpe, E. J. Fox, A. W. Barnard, J. Finney, K. Watanabe, T. Taniguchi, M. A. Kastner, and D. Goldhaber-Gordon, *Science* **365**, 605 (2019).
- [16] M. Serlin, C. L. Tschirhart, H. Polshyn, Y. Zhang, J. Zhu, K. Watanabe, T. Taniguchi, L. Balents, and A. F. Young, *Science* **367**, 900 (2020).
- [17] G. Chen, A. L. Sharpe, E. J. Fox, Y.-H. Zhang, S. Wang, L. Jiang, B. Lyu, H. Li, K. Watanabe, T. Taniguchi, Z. Shi, T. Senthil, D. Goldhaber-Gordon, Y. Zhang, and F. Wang, *Nature* **579**, 56 (2020).
- [18] T. Li, S. Jiang, B. Shen, Y. Zhang, L. Li, Z. Tao, T. Devakul, K. Watanabe, T. Taniguchi, L. Fu, J. Shan, and K. F. Mak, *Nature* **600**, 641 (2021).
- [19] E. Anderson, F.-R. Fan, J. Cai, W. Holtzmann, T. Taniguchi, K. Watanabe, D. Xiao, W. Yao, and X. Xu, *Science* **381**, 325 (2023).
- [20] Y. Xie, A. T. Pierce, J. M. Park, D. E. Parker, E. Khalaf, P. Ledwith, Y. Cao, S. H. Lee, S. Chen, P. R. Forrester, K. Watanabe, T. Taniguchi, A. Vishwanath, P. Jarillo-Herrero, and A. Yacoby, *Nature* **600**, 439 (2021).
- [21] Z. Ji, H. Park, M. E. Barber, C. Hu, K. Watanabe, T. Taniguchi, J.-H. Chu, X. Xu, and Z.-x. Shen, “Local probe of bulk and edge states in a fractional Chern insulator,” (2024), arXiv:2404.07157 [cond-mat].
- [22] Z. Lu, T. Han, Y. Yao, A. P. Reddy, J. Yang, J. Seo, K. Watanabe, T. Taniguchi, L. Fu, and L. Ju, “Fractional Quantum Anomalous Hall Effect in a Graphene Moire Superlattice,” (2023), arXiv:2309.17436 [cond-mat].
- [23] J. Dong, J. Wang, P. J. Ledwith, A. Vishwanath, and D. E. Parker, *Physical Review Letters* **131**, 136502 (2023), publisher: American Physical Society.
- [24] C. Wang, X.-W. Zhang, X. Liu, Y. He, X. Xu, Y. Ran, T. Cao, and D. Xiao, *Physical Review Letters* **132**, 036501 (2024).
- [25] J. Yu, J. Herzog-Arbeitman, M. Wang, O. Vafek, B. A. Bernevig, and N. Regnault, *Physical Review B* **109**, 045147 (2024), publisher: American Physical Society.
- [26] N. Morales-Durán, N. Wei, J. Shi, and A. H. MacDonald, “Magic Angles and Fractional Chern Insulators in Twisted Homobilayer TMDs,” (2023), arXiv:2308.03143 [cond-mat].
- [27] Y. Jia, J. Yu, J. Liu, J. Herzog-Arbeitman, Z. Qi, N. Regnault, H. Weng, B. A. Bernevig, and Q. Wu, “Moiré Fractional Chern Insulators I: First-principles calculations and Continuum Models of Twisted Bilayer MoTe₂,” (2023), arXiv:2311.04958 [cond-mat].
- [28] D. N. Sheng, A. P. Reddy, A. Abouelkomsan, E. J. Bergholtz, and L. Fu, “Quantum anomalous Hall crystal at fractional filling of moiré superlattices,” (2024), arXiv:2402.17832 [cond-mat].
- [29] J. Dong, T. Wang, T. Wang, T. Soejima, M. P. Zaletel, A. Vishwanath, and D. E. Parker, “Anomalous Hall Crystals in Rhombohedral Multilayer Graphene I: Interaction-Driven Chern Bands and Fractional Quantum Hall States at Zero Magnetic Field,” (2023), arXiv:2311.05568 [cond-mat].
- [30] T. Soejima, J. Dong, T. Wang, T. Wang, M. P. Zaletel, A. Vishwanath, and D. E. Parker, “Anomalous Hall Crystals in Rhombohedral Multilayer Graphene II: General Mechanism and a Minimal Model,” (2024), arXiv:2403.05522 [cond-mat].
- [31] H. Goldman, A. P. Reddy, N. Paul, and L. Fu, *Physical Review Letters* **131**, 136501 (2023), publisher: American Physical Society.
- [32] D. Vasyukov, Y. Anahory, L. Embon, D. Halbertal, J. Cuppens, L. Neeman, A. Finkler, Y. Segev, Y. Myasoedov, M. L. Rappaport, M. E. Huber, and E. Zeldov, *Nature Nanotechnology* **8**, 639 (2013).
- [33] Y. Anahory, H. R. Naren, E. O. Lachman, S. B. Sinai, A. Uri, L. Embon, E. Yaakobi, Y. Myasoedov, M. E. Huber, R. Klajn, and E. Zeldov, *Nanoscale* **12**, 3174 (2020).
- [34] C. L. Tschirhart, M. Serlin, H. Polshyn, A. Shragai, Z. Xia, J. Zhu, Y. Zhang, K. Watanabe, T. Taniguchi, M. E. Huber, and A. F. Young, *Science* **372**, 1323 (2021).
- [35] C. L. Tschirhart, E. Redekop, L. Li, T. Li, S. Jiang, T. Arp, O. Sheekey, T. Taniguchi, K. Watanabe, M. E. Huber, K. F. Mak, J. Shan, and A. F. Young, *Nature Physics*, 1 (2023).
- [36] S. Grover, M. Bocarsly, A. Uri, P. Stepanov, G. Di Battista, I. Roy, J. Xiao, A. Y. Meltzer, Y. Myasoedov, K. Pareek, K. Watanabe, T. Taniguchi, B. Yan, A. Stern, E. Berg, D. K. Efetov, and E. Zeldov, arXiv:2201.06901 [cond-mat] (2022).
- [37] T. Arp, O. Sheekey, H. Zhou, C. L. Tschirhart, C. L. Patterson, H. M. Yoo, L. Holleis, E. Redekop, G. Babikyan, T. Xie, J. Xiao, Y. Vituri, T. Holder, T. Taniguchi, K. Watanabe, M. E. Huber, E. Berg, and A. F. Young, “Intervalley coherence and intrinsic spin-orbit coupling in rhombohedral trilayer graphene,” (2023), arXiv:2310.03781 [cond-mat].
- [38] J. K. Jain, *Physical Review Letters* **63**, 199 (1989), publisher: American Physical Society.
- [39] T. Deilmann, P. Krüger, and M. Rohlfing, *Physical Review Letters* **124**, 226402 (2020), publisher: American Physical Society.
- [40] T. Woźniak, P. E. Faria Junior, G. Seifert, A. Chaves, and J. Kunstmann, *Physical Review B* **101**, 235408 (2020).
- [41] C. Robert, H. Dery, L. Ren, D. Van Tuan, E. Courtade, M. Yang, B. Urbaszek, D. Lagarde, K. Watanabe, T. Taniguchi, T. Amand, and X. Marie, *Physical Review Letters* **126**, 067403 (2021), publisher: American Physical Society.
- [42] R. Morf and B. I. Halperin, *Physical Review B* **33**, 2221 (1986).
- [43] F. Yang, A. A. Zibrov, R. Bai, T. Taniguchi, K. Watanabe, M. P. Zaletel, and A. F. Young, *Physical Review Letters* **126**, 156802 (2021).
- [44] J. Nakamura, S. Liang, G. C. Gardner, and M. J. Manfra, *Nature Physics* **16**, 931 (2020).

- [45] M. E. Huber, P. A. Neil, R. G. Benson, D. A. Burns, A. M. Corey, C. S. Flynn, Y. Kitaygorodskaya, O. Masihzadeh, J. M. Martinis, and G. C. Hilton, *IEEE Transactions on Applied Superconductivity* **11**, 1251 (2001).

METHODS

Device Fabrication

Devices used in this study are fabricated using methods previously described in the literature. Transport data from device A was previously reported in Ref. [2], where it appears as device “D(3.7°)”. Device B was previously studied in Ref. [4].

nSOT sensor fabrication and local magnetometry measurements

We perform magnetic imaging with a superconducting quantum interference device on the apex of a sharp quartz pipette (nSOT) [1, 32, 33]. We use a quartz micropipette with inner tube diameter of 0.5 mm to pull a sharp tip with the apex diameter of ≈ 150 nm. To form the coarse contacts, we deposit gold films by electron beam evaporation at a deposition rate of 2 \AA/s to produce a thickness of (50 \AA Ti/500 \AA Au). A shunt resistor is further deposited with (80 \AA Ti/150 \AA Au) within 500 μm from the tip apex, resulting in a $\approx 10 \Omega$ shunt resistance. We next cover the coarse contact pads with a thick layer of indium solder to minimize contact resistance and to improve contact with the leaf-springs used to hold the tip in the holder. We then evaporate indium in a home-built thermal evaporator at three angles to cover two contacts at 110° to the apex, with a head-on deposition performed last. The tip holder is mounted to a cryostat, and protected by radiation shielding and LN_2 jacketing; it is kept at a temperature of 20 K throughout the deposition process. Each evaporation step is preceded by 5–10 minutes of thermalization during which the evaporator chamber is flooded with He exchange gas at a pressure of 5×10^{-3} mbar. Typical thicknesses for the indium depositions are 350 \AA for the side contacts and 300 \AA for the head-on deposition for 150 nm tip diameter; we use a 1 \AA/s deposition rate for all steps. These parameters allow for a highly uniform, low grain-size film to form near the tip apex (see Extended Data Fig. 1a).

The magnetic field at the tip apex is read out by measuring the tip in a quasi-voltage bias configuration using a series SQUID array amplifier (SSAA) [45]. To calibrate the sensitivity of the nSOT we measure the frequency domain output of the SSAA amplifiers at the nSOT operating point. The nSOT voltage is converted to magnetic field via the transfer function, which we measure by monitoring the DC output voltage response to a $\sim 20 \mu\text{T}$ step in magnetic field. This gives the transfer function in units of V/T. As shown in Extended Data Fig. 1b, our nSOT sensors show a maximum sensitivity (typically near a flux bias point of $\Phi_0/2$) of $\approx 300 \text{ pT}/\sqrt{\text{Hz}}$ with an effective diameter of 200 nm, corresponding to $\approx 6 \text{ n}\Phi_0/\sqrt{\text{Hz}}$.

Magnetization reconstruction

To reconstruct the magnetization, we follow standard Fourier domain techniques (see, e.g., the supplementary information of reference [34]). The magnetization shown in the main text is computed by zero-padding the measured magnetic field map before Fourier transforms are computed. This constitutes an unphysical assumption about magnetic fields outside the measurement area that were not constrained experimentally—i.e., that they vanish—and constitutes a source of systematic error.

To address this source of error in m , we analyze the influence of the choice of padding on the reconstructed magnetization, shown in Extended Data Fig. 7. Our base model assumes zero magnetic field outside the region where the fields are measured. We then compare this to two alternative assumptions: first, we replicate the signal between the contacts on the left and right sides of the frame, extending the finite magnetic fields observed at the boundary into a region 500 nm wide. As a second comparative model, we extend the fields on the edge of this region by an additional 500 nm above and below the measured region. As shown in the figure, the reconstructed magnetization differs from the base model by $\sim 10\%$ in the neighborhood of both $\nu = -1$ and $\nu = -2/3$, with comparable or smaller effects on the inferred gap size.

Measurement conditions for presented data

All voltages indicated denote root-mean-square values.

- Fig. 1a, Extended Data Figs. 2e, 6
Transfer function = 100 V/T;
height = 150 nm;
 $\delta V_s = 20 \text{ mV}$;
frequency = 511.777 Hz
- Fig. 1b,c, Extended Data Figs. 2d, 4, 5
Transfer function = 250 V/T;
height = 100 nm;
 $\delta V_t = 40.1 \text{ mV}$; $\delta V_b = 35.8 \text{ mV}$;
frequency = 151.777 Hz
- Fig. 1d,e
Transfer function = 500 V/T;
height = 50 nm;
 $\delta V_t = 4.1 \text{ mV}$; $\delta V_b = 3.6 \text{ mV}$;
frequency = 511.777 Hz
- Fig. 1f
Transfer function = 500 V/T;
height = 50 nm;
 $\delta V_t = 40.1 \text{ mV}$; $\delta V_b = 35.8 \text{ mV}$;
frequency = 90.777 Hz

- Fig. 1f inset

Transfer function = 500 V/T;
 height = 50 nm;
 $\delta V_t = 20$ mV; $\delta V_b = 18$ mV;
 frequency = 90.777 Hz

- Fig. 2, Fig. 3c,d,f, Fig. 4a,b

Transfer function = 280 V/T;
 height = 150 nm;
 $\delta V_b = 40$ mV;
 frequency = 511.777 Hz

- Fig. 3a,b

Transfer function = 500 V/T;
 height = 100 nm;
 $\delta V_s = 5$ mV;
 frequency = 151.777 Hz

- Fig. 4d

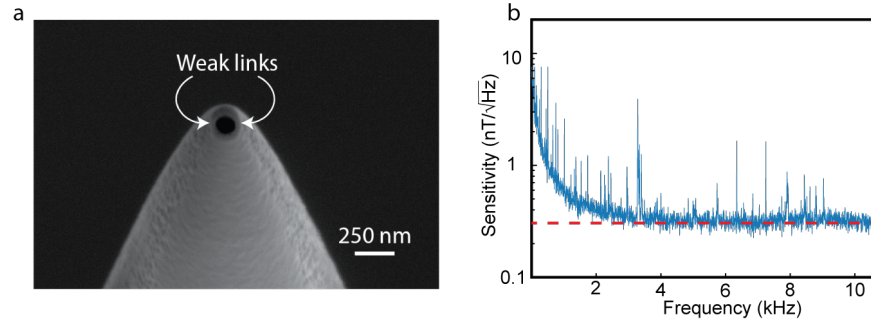
Transfer function = 500 V/T;
 height = 50 nm;
 $\delta V_t = 60.6$ mV; $\delta V_b = -53$ mV;
 frequency = 1151.777 Hz

- Extended Data Fig. 2f

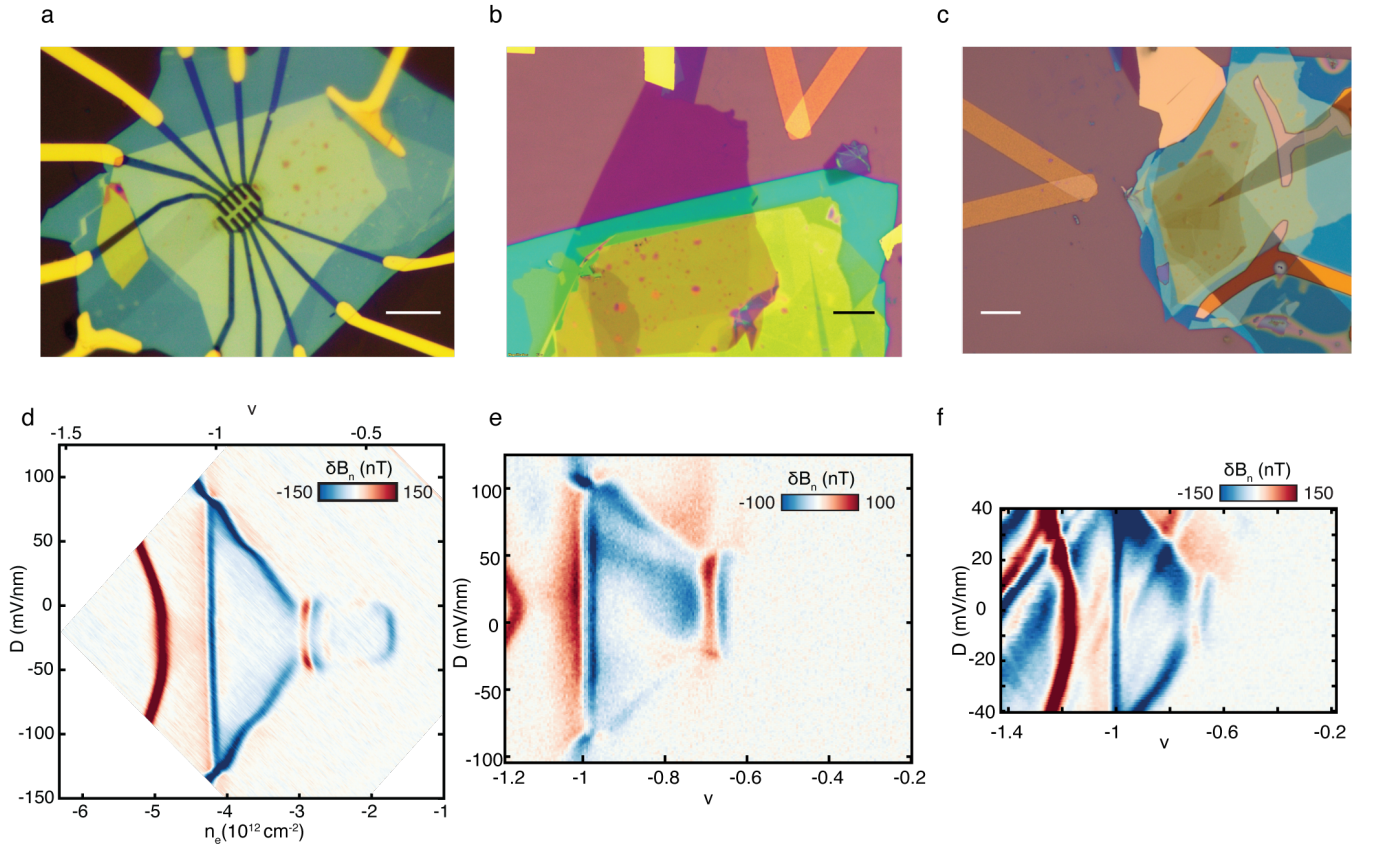
Transfer function = 100 V/T;
 height = 180 nm;
 $\delta V_s = 28$ mV;
 frequency = 251.777 Hz

- Extended Data Fig. 3

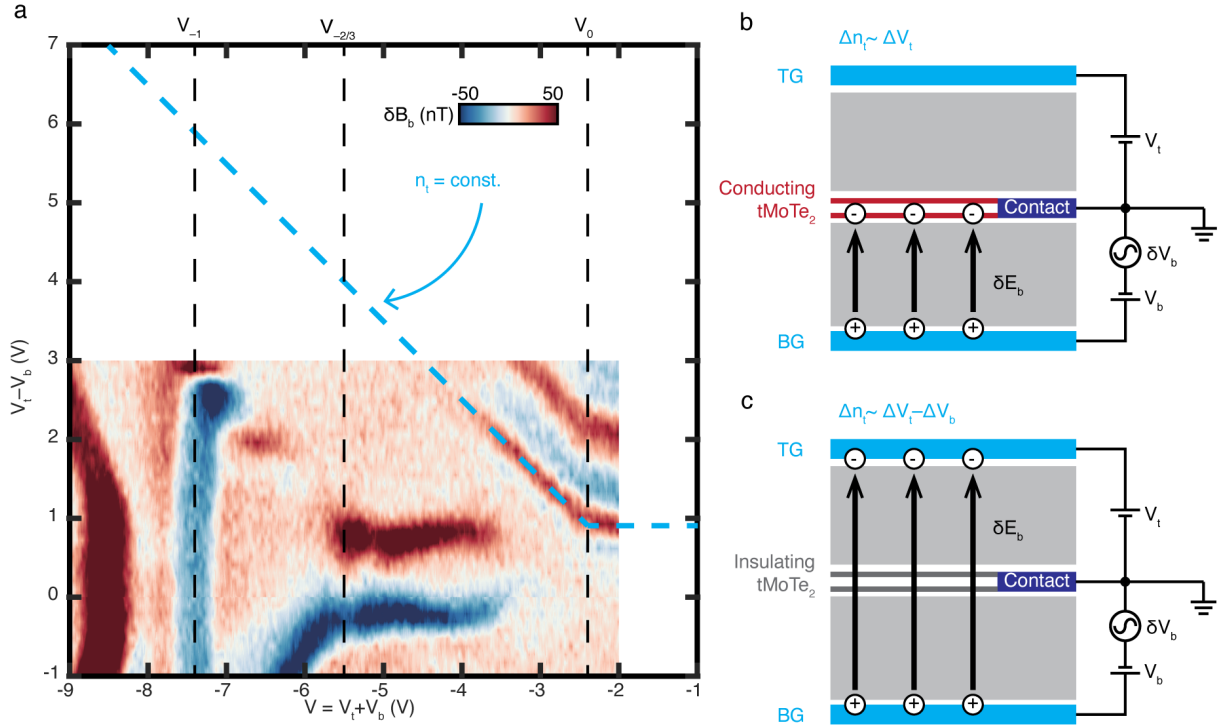
Transfer function = 500 V/T;
 height = 100 nm;
 $\delta V_b = 28$ mV;
 frequency = 251.777 Hz



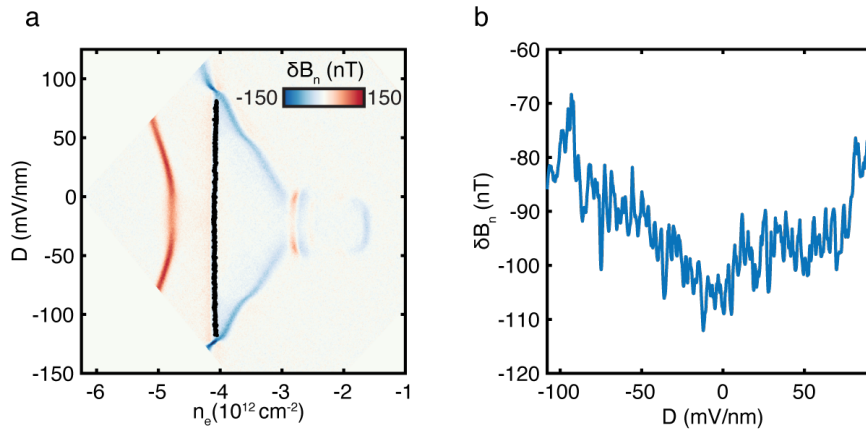
Extended Data Fig. 1. SQUID sensitivity (a) SEM image of the nSOT sensor used in most of the current work, highlighting the superconducting weak links on the tip apex. (b) Typical sensitivity of the nSOT as a function of the frequency. $1/f$ noise dominates at frequencies below 1 kHz and decays below the instrumentation noise floor above 2 kHz allowing for ultra-high magnetic field sensitivity well below $1\text{ nT}/\sqrt{\text{Hz}}$.



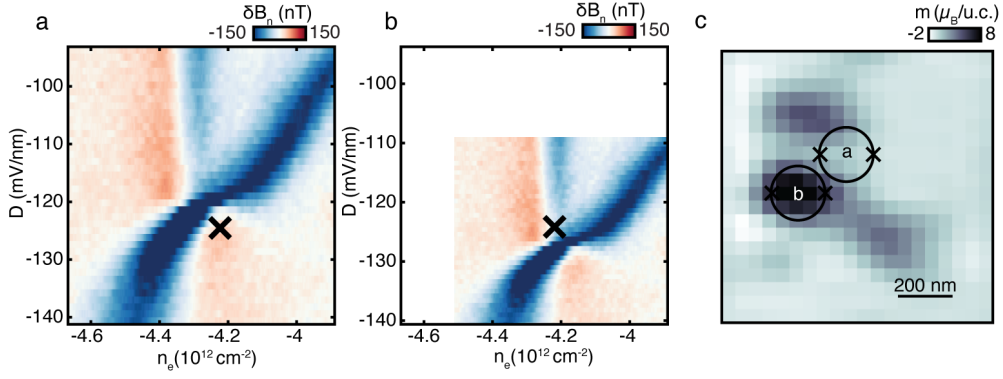
Extended Data Fig. 2. Devices (a) Optical micrograph of Device A (corresponding to device D(3.7°) from Ref. [2]); (b) Device B (corresponding to device from Ref. [4]); (c) Device C. Scale bar is $10\ \mu\text{m}$; (d) δB_n phase diagram measured in Device A, (e) Device B, and (f) device C. All devices show signals near $\nu = -1$ and $\nu = -2/3$ characteristic of Chern insulators.



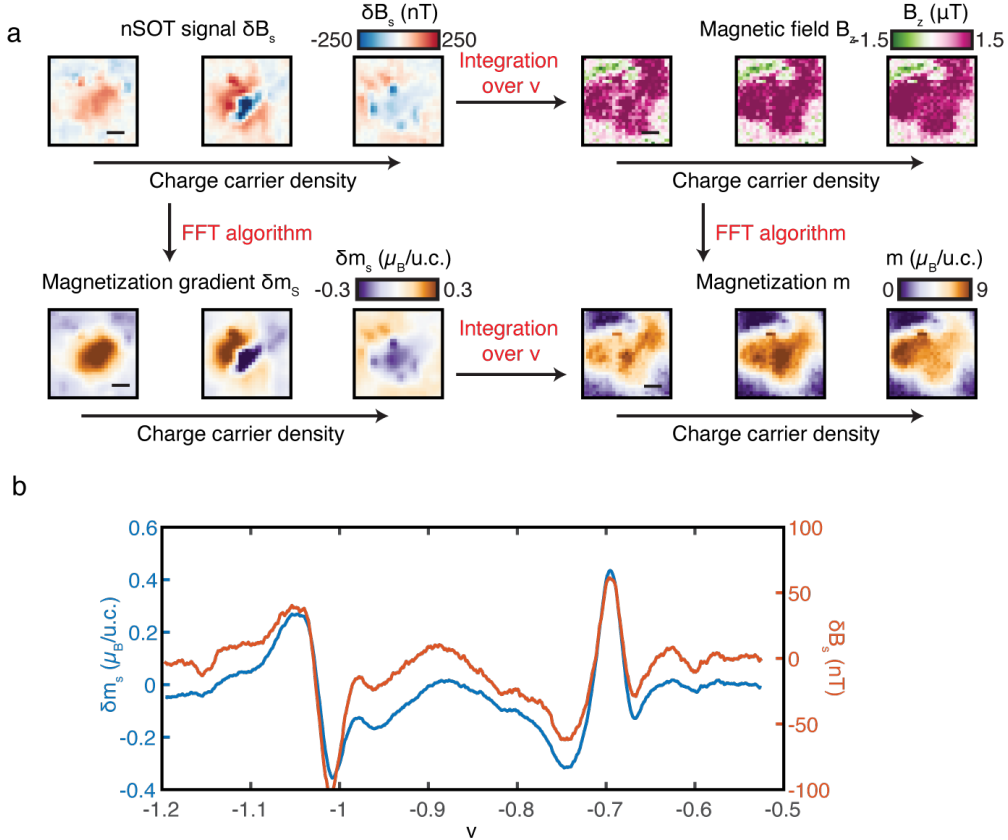
Extended Data Fig. 3. Chemical potential sensing and band edge offset. (a) δB_b for device C as a function of $V \equiv V_t + V_b$ and $V_t - V_b$ exhibiting both MoTe₂ features described in the main text as well as features associated with Landau levels of the top graphite gate. The band edge is visible as a kink in the constant top gate carrier density trajectory, marked as a dashed blue line, with the offset V_0 corresponding to the voltage that separates the regime where tMoTe₂ is insulating and the regime where it is hole-doped. The value obtained using this method agrees with that described in the main text using the $\nu = -1$ and $\nu = -2/3$ gap densities. (b) Schematic of the electric field in the hole-doped tMoTe₂ regime. Here modulations of the bottom gate produce electric fields δE_b which are screened by the tMoTe₂ layer. In this regime, the top gate density n_t is tuned solely by V_t , and trajectories of constant n_t follow slope -1 on the diagram in panel a. (c) Schematic of the electric field in the insulating tMoTe₂ regime. Here δE_b penetrates the tMoTe₂, so that n_t is tuned by both V_t and V_b . In this regime, constant- n_t lines have slope 0 in panel a.



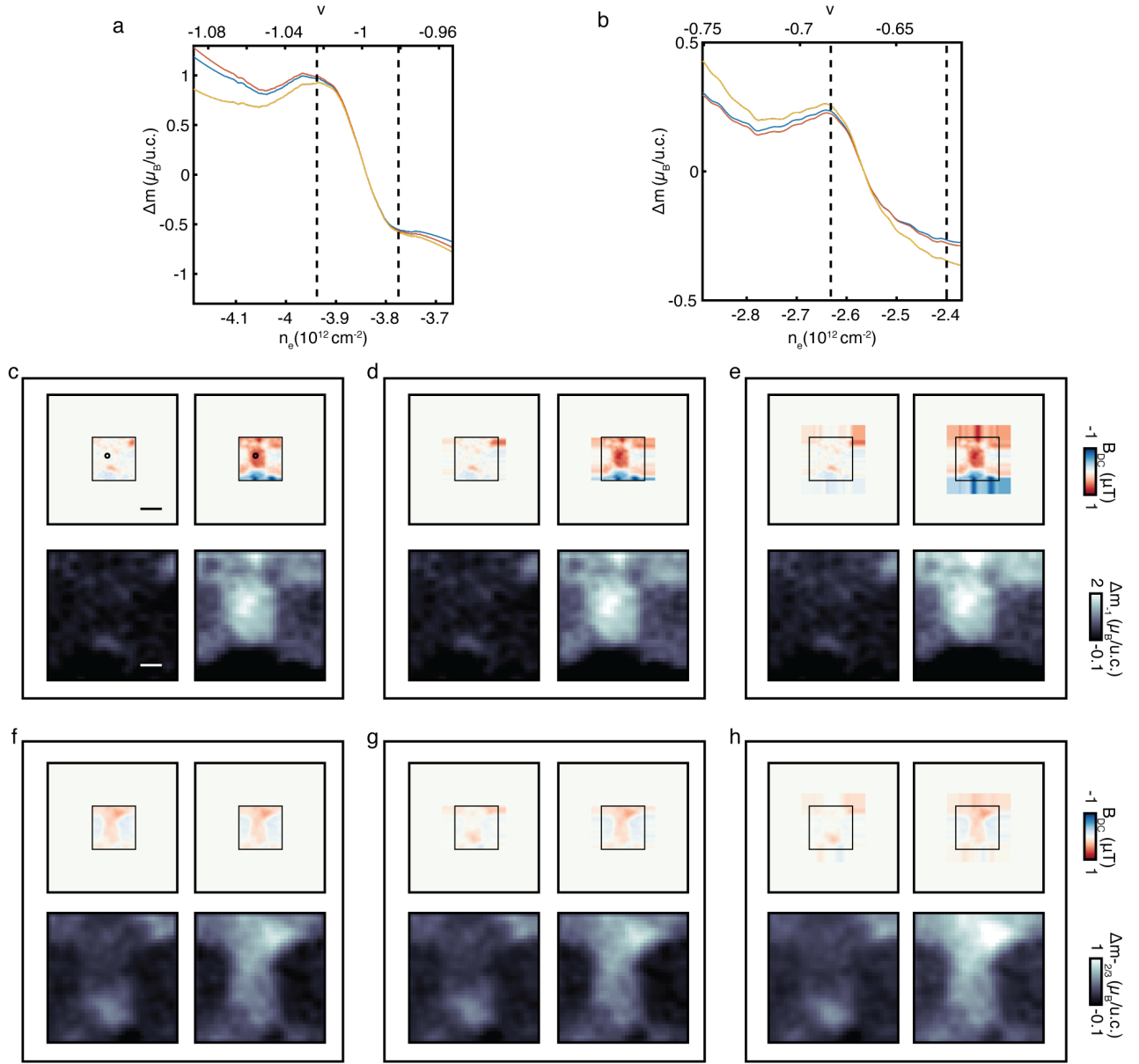
Extended Data Fig. 4. Chern insulator signal dependence on the displacement field (a) Signal δB_n as a function of charge carrier density and electric displacement field; (b) Minimum value of δB_n in a window around $\nu = -1$ gap along displacement field axis. The positions of the values are shown on a. The signal from the gap decays slightly as a function of displacement field, remaining finite up to the first order phase transition induced by layer polarization.



Extended Data Fig. 5. First order valley polarization transition at $\nu = -1$ (a) δB_n near the valley polarization transition in the vicinity of $\nu = -1$ at point “a” in panel c. (b) δB_n measured at point “b”, 200 nm away from point “a”. Both panel a and b show a sharp first-order-like signal on the boundary of the $\nu = -1$ Chern insulator peak, but these transitions appear at slightly different values of D and n_e . (c) Reconstructed magnetization in the point indicated by the “x” on panels a and b. The measured measured m at position “a” is consistent with zero to within our experimental error, and we find no evidence for non-zero net magnetization in the high $|D|$ phases. The non-zero signal observed in δB_n at that position is associated with fringe AC magnetic fields arising from areas where where the “x” position in parameter space corresponds to the valley transition.



Extended Data Fig. 6. Magnetization reconstruction. (a) Schematic of analysis to reconstruct the magnetization. We measure the local magnetic field δB_s in response to a modulated sample voltage δV_s ; data is from Device B, with scale bar of $2 \mu\text{m}$. An FFT-based algorithm (see Methods) can be used to directly compute the corresponding δm_s , which may then be integrated over V_s to obtain m . Alternatively, the δB_s signal may be integrated over V_s to obtain B , which can in some cases be compared to the directly measured B_{DC} ; this can then be processed by the FFT algorithm to produce the same m . (b) Comparison of the measured δB_s (orange) and the reconstructed δm_s (blue) as a function of the filling factor ν at a single given spatial location. While qualitative features are preserved, but of course quantitative features differ.



Extended Data Fig. 7. Estimating systematic error due to padding assumptions. (a) Magnetization change Δm (referenced to the center of the $\nu = -1$ gap) in the same location as that shown in Fig. 3 for the three different padding assumptions described in panels c, d, and e. (b) Magnetization change Δm (referenced to the center of the $\nu = -2/3$ gap) in the same location as that shown in Fig. 3 for the three different padding assumptions described in panels f, g, and h. (c) Top row: measured B_{DC} with zero padding assumption across the $\nu = -1$ gap. Scale bar is 600 nm. Left and right panels correspond to n_e values shown by dotted lines in panel a. Bottom row: reconstructed magnetization in the measured range at the same positions, with the zero padding assumption. The magnetization change across the gap is $1.44 \mu_B/\text{u.c.}$ Scale bar is 200 nm. (d) Same as panel c, except with the padding assumption that data extends to the right and left of measured area as shown. The magnetization change across the gap is $1.48 \mu_B/\text{u.c.}$ (e) Same as panels c and d but with additional padding as shown. Magnetization change across the gap is $1.41 \mu_B/\text{u.c.}$ (f) Top row: measured B_{DC} with zero padding assumption across the $\nu = -2/3$ gap. Left and right panels correspond to n_e values shown by dotted lines in panel b. Bottom row: reconstructed magnetization in the measured range at the same positions, with the zero padding assumption. The magnetization change across the gap is $0.46 \mu_B/\text{u.c.}$ (g) Same as panel f, with the same padding assumption as panel d. Magnetization change across the gap is $0.46 \mu_B/\text{u.c.}$; (h) Same as panels f-g but with the same padding assumption as in panel e. Magnetization change across the gap is $0.51 \mu_B/\text{u.c.}$